



Regulation of energetic hot carriers on Pt/TiO₂ with thermal energy for photothermal catalysis

Jinqiang Zhang^{a,b}, Yunguo Li^c, Jiaming Sun^a, Haijun Chen^{a,*}, Yuezhao Zhu^a, Xiaoli Zhao^b, Lai-Chang Zhang^b, Shuaijun Wang^b, Huayang Zhang^d, Xiaoguang Duan^d, Lei Shi^e, Shu Zhang^e, Peng Zhang^f, Guosheng Shao^f, Mingbo Wu^g, Shaobin Wang^{d,*}, Hongqi Sun^{b,*}

^a Jiangsu Key laboratory of Process Enhancement and New Energy Equipment Technology, School of Mechanical and Power Engineering, Nanjing Tech University, Nanjing 211816, Jiangsu, China

^b School of Engineering, Edith Cowan University, 270 Joondalup Drive, Joondalup, WA 6027, Australia

^c School of Earth and Planetary Sciences, University of Science and Technology of China, Hefei, China

^d School of Chemical Engineering, The University of Adelaide, Adelaide, SA 5005, Australia

^e College of Materials Science and Engineering, Nanjing Forestry University, 210037 Nanjing, China

^f School of Materials Science and Engineering, Zhengzhou University, Zhengzhou 450001, China

^g State Key Laboratory of Heavy Oil Processing, Institute of New Energy, College of Chemical Engineering, China University of Petroleum (East China), Qingdao 266580, China

ARTICLE INFO

Keywords:

Photothermal catalysis
Thermal energy
Energetic hot carriers
Onset reaction temperature
Dry reforming of methane
Carbon dioxide reduction

ABSTRACT

Thermal and solar energies are two pivotal components in photothermal catalysis, however, their synergistic energy efficiency for a maximum yield is more important but less investigated. Herein, systematic studies unveil the promotion effects of external heat on the excitation and utilization of energetic hot carriers (EHC) on Pt/TiO₂ in photothermal catalysis. Onset reaction temperature of a reaction is found to be the key in control of the energy synergy. When the minimum onset reaction temperature of uphill processes is exceeded, a smaller number of active sites on the catalyst are available to EHC, resulting in a suppressed thermal effect. Rational regulation of EHC and thermal energy in photothermal catalysis leads to optimum quantum efficiencies of both dry reforming of methane and reverse water-gas shift reactions at a medium level of temperature. This work provides new insights to balance thermal and solar-driven catalysis to better conduct photothermal catalysis for fossil fuels upgrading.

1. Introduction

Semiconductor-based photocatalysis emerged amid the energy crisis in 1970s and thereafter it has been deemed as a promising strategy towards conversion and storage of solar energy into chemical stocks [1]. To date, the quantum efficiency (QE) of photocatalysis is still unsatisfied despite of numerous studies in the past decades [2,3], attributing to the intrinsic low energy of directly photoexcited hot carriers [4]. Photothermal catalysis via integrating hot-carriers-driven photocatalysis with thermocatalysis holds a promise to a large-scale solar energy utilization [5,6]. In the photochemical process, parts of photo-excited hot carriers on the surface of nanometals are more energetic, namely energetic hot carriers (EHC) [7,8], which can directly initiate tough processes at mild conditions, leading to an intriguing solar-to-fuel efficiency [9–11]. It

should also be noted that desirable selectivity of target products can be realized with the participation of photo-induced EHC [12,13]. While other hot carriers with relatively low energy would decay to internal thermal heat via Ohmic damping and fail to participate in the redox reactions, resulting in a temperature increase on the catalyst surface [14]. Therefore, according to the van't Hoff equation, a reaction can also be accelerated at the elevated temperature. In an inspiring study, Shoji et al. reported that the apparent QE of photothermal catalytic dry reforming of methane (DRM) can be improved to 5.9% over a SrTiO₃-supported rhodium catalyst at ambient conditions [15].

Towards a further success, however, one of the challenges is that the increased catalyst temperature from internal thermal energy is usually lower than the minimum onset temperature of thermocatalysis. Generally, group-VIII metals are effective for thermocatalytic DRM and can

* Corresponding authors.

E-mail addresses: chenhj@njtech.edu.cn (H. Chen), shaobin.wang@adelaide.edu.au (S. Wang), h.sun@ecu.edu.au (H. Sun).

<https://doi.org/10.1016/j.apcatb.2022.121263>

Received 2 January 2022; Received in revised form 20 February 2022; Accepted 25 February 2022

Available online 27 February 2022

0926-3373/© 2022 Elsevier B.V. All rights reserved.

also response to solar light to generate hot carriers [13,16,17]. External heating has also been introduced into group-VIII metal based photothermal catalysis to enable thermocatalysis [5,18]. This concept was evidenced by the significantly enhanced performances of some thermodynamically endothermic reactions, for examples, DRM [19] and reverse water gas shift (RWGS) reaction [20] at a rate of as high as mmol/h/g, or even mol/h/g [21]. EHC and external thermal energy have been respectively proven their effectiveness in photothermal catalysis, however, the synergy of EHC and external thermal energy is not well probed. Current attentions are more paid on development of photothermal catalysts, while unveiling the ceiling of solar and thermal energy utilization in photothermal catalysis is of equal importance. As such, understanding the interactions between thermal energy and EHC for a maximum utilization of their contributions in photothermal catalysis would be the key to save energy consumption and optimize the overall photothermal catalytic efficiency.

Herein, we will attempt to establish the correlation between the hot region (the area accumulated with the most EHC) and external heating temperature over a Pt quantum dots/commercial TiO₂ (Pt/P25) catalyst in photothermal catalysis. Combined with experimental and computational results, a positive effect of thermal energy on EHC in photothermal catalytic DRM and RWGS was observed, in terms of both excitation and output (utilization of EHC for redox reactions). However, a suppression effect of thermal energy on the output of EHC was found after the reaction temperature exceeded the minimum onset temperature of thermocatalytic uphill reactions. With such an insight, both DRM and RWGS reactions were carried out at a medium level of temperature to achieve the optimized QEs, as high as 56% at 500 °C and 20% at 400 °C under 420 nm, respectively. The highest photothermal catalytic throughput was attained at high temperature with a less photo quantum efficiency, and with corresponding turnover frequency (TOF) of 5.1 mol CO/(mol Pt)/s of DRM at 700 °C and 1.0 mol CO/(mol Pt)/s of RWGS at 500 °C. This study offers the key to regulate photothermal catalysis for better and rational energy utilization and upgrading of fossil fuels.

2. Experimental section

2.1. Catalyst preparation

Commercial TiO₂ (P25) (0.2 g) and ethylene glycol (50 mL) were mixed into a three-neck flask followed by ultrasonication in 15 min for good dispersion. Subsequently H₂PtCl₆·6H₂O/ethylene glycol (2.1 mL, 5 mg mL⁻¹) solution was dropwise added into the flask. After 1 h vigorous stirring, the flask was sealed and purged with N₂ for several times. A NaOH/ethylene glycol solution (1.25 mL, 0.25 M) was then injected into the flask, which was then heated at 160 °C for 2 h. After the flask cooling down to ambient temperature, an HCl/ethylene glycol solution (2 mL, 0.25 M) was injected into the flask with stirring for another 2 h. The obtained sample was respectively washed with ethanol and H₂O for several times. Finally, the product was kept in a vacuum oven overnight. The whole catalyst preparation process was conducted without light exposure.

2.2. Characterizations

X-ray diffraction (XRD) (X'Pert PRO MPD, Holland) was employed for the characterization of the crystal structures of the samples. The morphology was monitored on a JEOL 2100. High-angle annular dark-field scanning transmission electron microscopy (HAADF-STEM) and energy-dispersive X-ray (EDX) elemental mapping was recorded on a FEI Titan G2 80–200 TEM/STEM. *In situ* irradiation X-ray photoelectron spectroscopy (XPS) measurements were conducted on a Shimadzu AXIS Supra instrument with Al K α irradiation. The binding energy was calibrated with C 1 s signal (284.6 eV) as the reference. The wavelength of the UV-light source was 365 nm and the power was 300 W. A Cary 100 UV-Vis Spectrophotometer was used for recording the diffused

reflectance spectra. Electron paramagnetic resonance (EPR) spectra with *in situ* light irradiation were acquired on a Bruker A300–10/12 and *in situ* time-resolved decay spectra were recorded on a FLS1000 (the temporal resolution of the time resolved decay measurement is 305 fs). *In situ* diffuse reflectance infrared Fourier transform spectroscopy (DRIFTS) was performed on a Bruker VERTEX 70 V with a 300 W Xe lamp as the light source.

2.3. Photothermal and thermal catalytic dry reforming of methane reactions

The photothermal catalytic DRM was carried out in a self-designed reactor equipped with an overhead Xenon lamp. At first, 20 mg catalyst was uniformly coated on a quartz microfiber filter. Before reaction, the catalyst was activated by H₂ at 700 °C for 1 h. After cooling down to ambient temperature, the reactor was flushed by Ar to evacuate the residual H₂. Then the reaction gases (CH₄/CO₂/Ar = 48/48/4) were introduced into the reactor at a flow rate of 20 mL/min until the reactor was filled with the feed gases. The reaction was initiated by turning on the light. In the meantime, a thermocouple under the catalyst bed was used to record the average temperature of catalysts during the reaction. Then the performances of photothermal/thermo-catalytic DRM at the external heating temperature of 300, 500 and 700 °C were evaluated via adjusting the furnace temperature. The effluent gases were analyzed online by a gas chromatography (GC, Agilent 7820A) equipped with Porapak N and Molsieve 5A columns. Thermocatalytic performances for DRM at the same catalyst bed temperature as photothermal catalysis were also tested.

2.4. Photothermal and thermocatalytic CO₂ reduction with H₂

The pretreatment of a catalyst in CO₂ reduction reaction with hydrogen was similar to that of DRM process. After the activation of the catalyst, reaction gases (H₂/CO₂/Ar = 72/24/4) were introduced into the reactor at a flow rate of 20 mL/min until the reactor was filled with the feed gases. The reaction was initiated by turning on the light. In the meantime, a thermocouple under the catalyst bed was used to record the average temperature of catalyst during the reaction. Then the photothermal/thermo-catalytic performances were evaluated at the external heating temperature of 100, 300 and 500 °C, respectively. Thermocatalytic performances for CO₂ reduction reaction with hydrogen at the same catalyst temperatures as photothermal catalysis were also measured.

2.5. Light effect on thermocatalytic DRM and CO₂ reduction performance

At first, the light was turned on and off every one hour in the DRM process at the external heating temperature of 700 °C and CO₂ reduction with hydrogen reaction at the external heating temperature of 500 °C to study the light effect on the thermocatalytic performances. Then the irradiations with different bandpass filters (> 420 and > 490 nm) and with different light intensities (5.0, 4.6 and 4.2 W/cm²) were added into the DRM process at the external heating temperature of 700 °C and CO₂ reduction with hydrogen at the external heating temperature of 500 °C, respectively, to investigate the light effect on the thermocatalytic reactivity. At last, the irradiations with different shortpass filters (420 and 500 nm) were introduced into the DRM process at the external heating temperature of 700 °C and CO₂ reduction with hydrogen at the external heating temperature of 500 °C to record their quantum efficiencies in photothermal catalysis.

2.6. Density function theory (DFT) calculations and finite element modelling (FEM)

We used the CASTEP code for DFT calculations [22]. A plane-wave basis set, together with the Perdew-Burke-Ernzerhof (PBE) type of

generalized gradient approximation (GGA) was used [23]. The Brillouin zone was sampled with $3 \times 3 \times 4$ k-point, and the cut off energy was set to 340 eV. Periodic Pt lattice was constructed with a lattice parameter of 0.27744 nm for the parallelepiped primitive cell [24]. The lattice parameters were then scaled, using a thermal expansion coefficient in the reference [24], to obtain the results for higher temperature. The results of complex permittivity were first obtained from the calculations, and then the complex refractive indices were evaluated from the equations below.

$$n = \sqrt{\frac{|\epsilon| + \epsilon}{2}} \text{ and } \kappa = \sqrt{\frac{|\epsilon| - \epsilon}{2}} \quad (1)$$

Where, n and κ are the real and imaginary parts of the refractive index, respectively, and ϵ is the complex permittivity.

In this work, finite element modelling (FEM) was carried out to evaluate the absorption coefficient of a Pt thin film, using the COMSOL software. A planar thin film of 10 nm was placed horizontally within a standard electric-magnetic radiation modelling space. Electro-magnetic radiation of different wavelengths (300–700 nm) was transmitted from the top downwards. Perfect matching layers were set at the top and bottom, and periodic boundaries at the sides [25]. The radiation fields were modelled by solving Maxwell equations. The absorption coefficient of the film was then evaluated by averaging the fraction of the output flux over the incident flux across the wavelength range.

3. Results and discussion

3.1. Catalyst characterizations

We chose Pt loaded commercial TiO₂ (P25) as a catalyst to study the thermal effects in photothermal catalytic processes, mainly because of its dual function as both an efficient photo responsive catalyst [7,26] and a typical thermocatalyst [27]. After an acid-base-mediated ethylene glycol reduction, Pt nanoparticles (NPs) are uniformly loaded on the surface of P25 (Fig. S1), with the facet of face center cubic (fcc) Pt (111) exposed (the characteristic peak located at $2\theta = 39.7^\circ$ in Fig. 1a) [28]. It has been reported that, as the size of the metal NPs reduced below 10 nm, a size related quantum effect starts imposing the significant influence over the behaviors of the plasmonic reactions to the light field [29]. As such, Pt nanoparticles with an average size of ~ 3 nm is named as Pt quantum dots (QDs) (Fig. S2), and Pt QDs loaded P25 catalyst is here named as Pt/P25. Pure P25 can only absorb UV light due to a wide band gap. After Pt loading, the light absorption of Pt/P25 is appreciably enhanced throughout the visible light spectrum (Fig. 1b). The optical enhancement is attributed to the strong light absorption ability of loaded Pt QDs, which would lead to the generation of EHC via the interband or intraband for the direct participation of redox reactions [16]. Once hot carriers on Pt QDs fail to reduce/oxidize reactants, they would decay to internal heat owing to the Ohmic damping [30]. In this study, the temperature of catalyst bed was *in situ* monitored during the photothermal catalytic DRM and CO₂ reduction with H₂ processes, in which the average temperature of the catalyst bed increased as the reactions progressed (Fig. 1c). It suggests that both EHC and converted internal thermal energy existed in the photothermal catalysis.

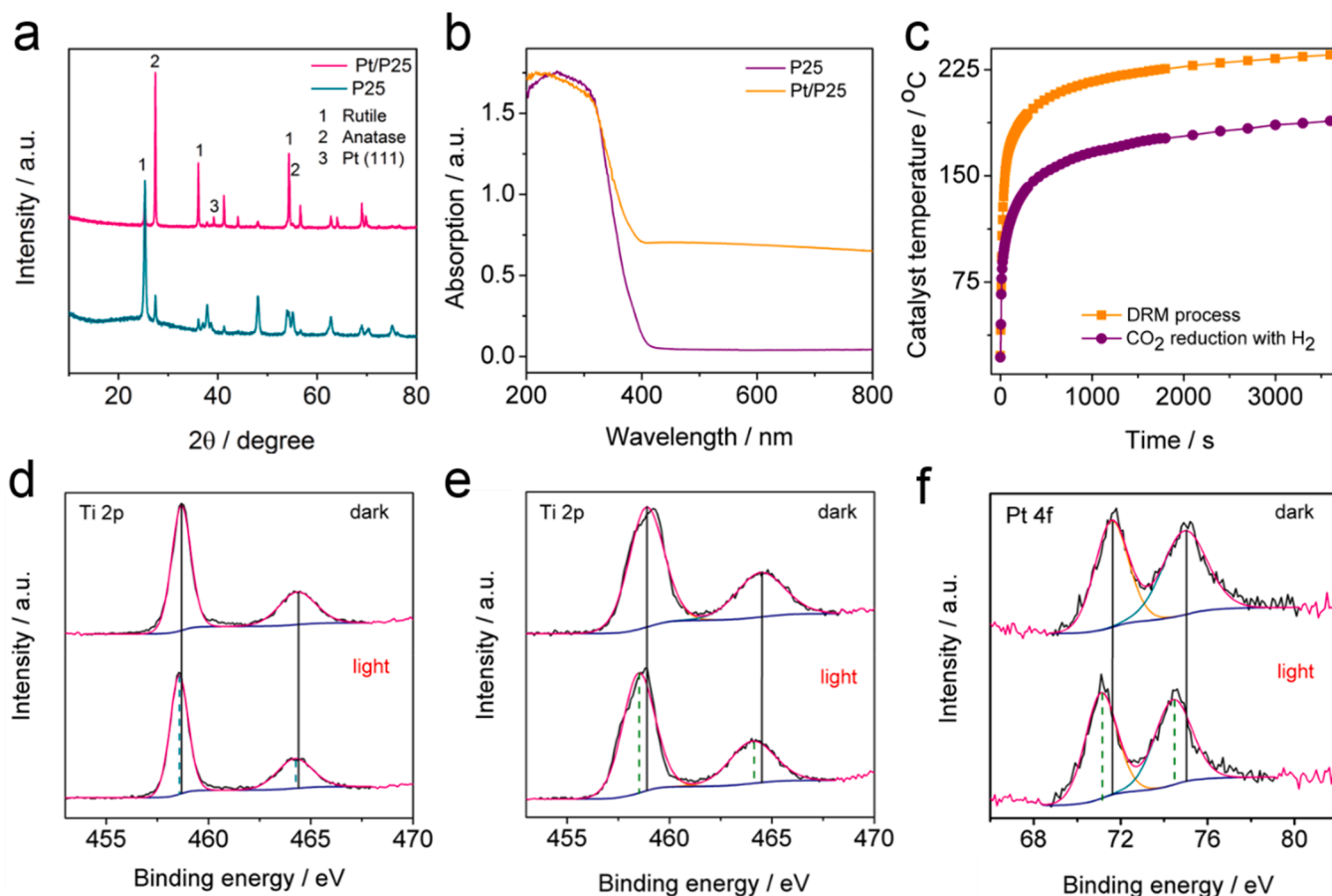


Fig. 1. Catalyst characterizations. (a) XRD patterns and (b) UV-Vis spectra of P25 and Pt/P25. (c) In situ monitored catalyst temperature of Pt/P25 in the photothermal catalytic DRM and CO₂ reduction with H₂ processes without external heating. XPS spectra of P25 and Pt/P25 with and without *in situ* light irradiations, Ti 2p of (d) P25 and (e) Pt/P25 and (f) Pt 4f of Pt/P25.

3.2. Temperature-dependent hot region on Pt/P25

A hot region is known as the accumulation area of hot carriers in photocatalysis, where most EHC on a photocatalyst participate into redox reactions. As such, we first employed *in situ* techniques to observe the temperature-dependent hot region on P25 and Pt/P25. XPS and EPR with both *in situ* light irradiations were used to study the dynamics of photo induced hot carriers at room temperature. As demonstrated from XPS spectra with *in situ* light irradiations, the binding energy of Ti 2p slightly decreased upon light irradiation, indicating the photogeneration of electron-hole pairs (Fig. 1d). When Pt QDs were loaded, an appreciable red-shift was observed in Ti 2p spectra upon light irradiation, similar to the case of Pt 4f spectra (Fig. 1e-f and Table S1). The shift in Pt 4f spectrum means that the kinetic energy of free electrons on Pt is enhanced after light irradiation, while the more distinct shift of Ti 2p after Pt loading suggests that the electron with sufficient energy on Pt QDs would overcome the Schottky barrier (formed between P25 and Pt) to migrate onto bulk P25, forming an enhanced electrical field within the metal-support interface at room temperature [31]. Another evidence of hot electron transferring from Pt to P25 can be seen from the EPR results with *in situ* light irradiation. The double integration area of peak in EPR result represents the concentration of hot electrons. As compared with P25, the captured number of hot electrons in Pt/P25 was increased, further suggesting that parts of the hot electrons on Pt would move to bulk P25 (Fig. 2a and S3a). The observation is consistent with a previous study [32].

We then applied time-resolved decay spectra (excited at 375 nm and probed at 441 nm) with *in situ* heating to observe the behavior of hot carriers at elevated temperature (Fig. 2b). The average lifetime of hot electrons turned longer from 1.819 to 2.023 ns with temperature increased from 127 to 177 °C. The prolonged lifetime suggests that the excited hot electrons at 177 °C could move farther than those at 127 °C

[33]. On the contrary, the average lifetime becomes slightly shorter (2.015 ns) at 227 °C as temperature further increases. Therefore, the transfer rate of hot electrons turns slow at high temperature. In theory, the mobility of hot electrons depends on their interactions with both phonons and impurities. A more thorough analysis of the scattering of electrons by phonons yields the following dependence of mobility (μ_T) on temperature:

$$\mu_T \propto T^{-3/2} \quad (2)$$

and the dependence of mobility (μ_N) on impurity concentration (N).

$$\mu_N \propto \frac{T^{3/2}}{N} \quad (3)$$

When the dependence on both the temperature and impurities is taken into account, the mobility, μ , is given as follows.

$$\frac{1}{\mu} = \frac{1}{\mu_T} + \frac{1}{\mu_N} \quad (4)$$

As such, with a stepwise increase in temperature, impurity predominates firstly and then photon effect takes over the control on the electron mobility, leading to an increase before 177 °C and then a decrease thereafter in the average lifetime of hot electrons. This is well consistent with the trends revealed from time-resolved decay spectra. The EPR results with *in situ* light irradiations and heating echoed using the double integration which represents the concentration of hot electrons on the catalyst support (Fig. 2c-d and S3b-c). With temperature rising from room temperature to 100 °C, an increased number of hot electrons is acquired on Pt/P25. However, the concentration of hot electrons on Pt/P25 drops when the temperature further increases to 300 °C, meaning fewer hot electrons can be captured on bulk P25. Therefore, hot electrons on Pt QDs would prefer to stay on Pt surface for redox reactions. This is consistent with the change pattern of the average

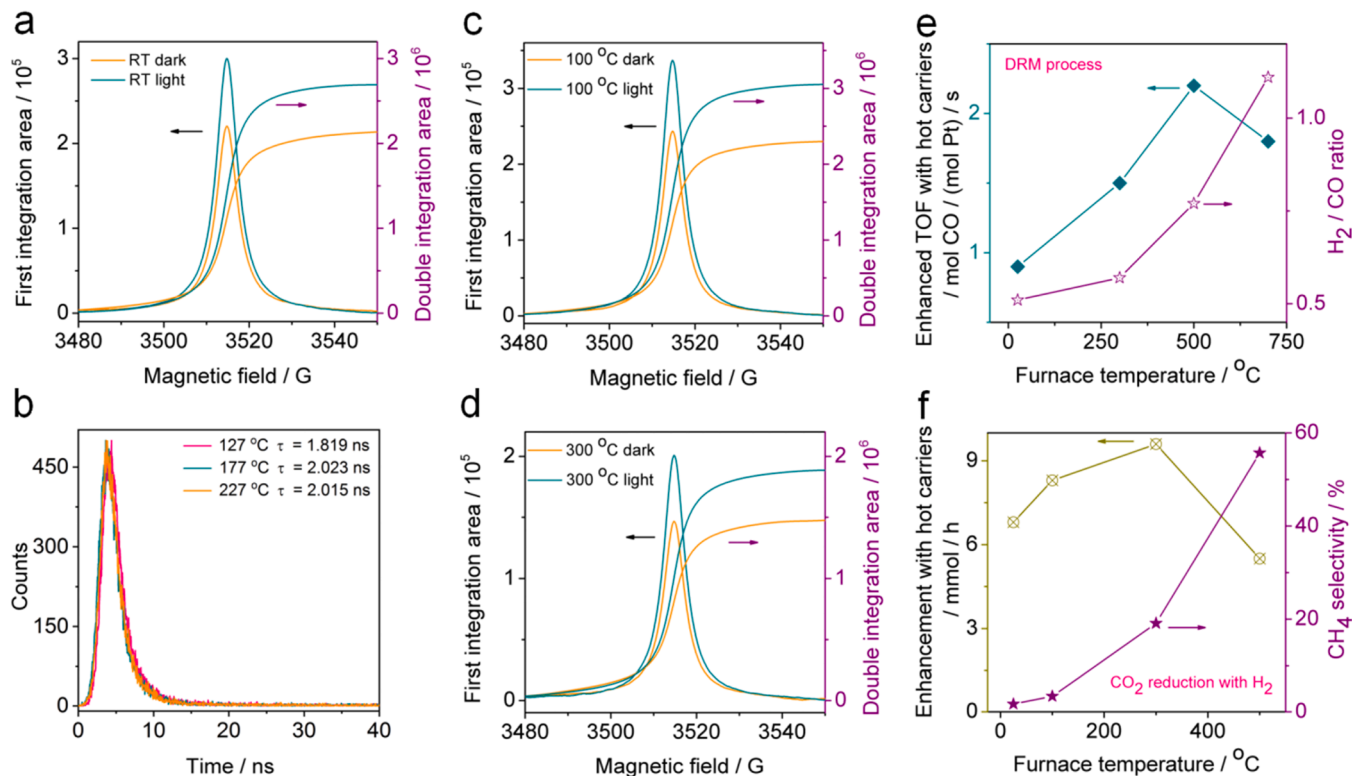


Fig. 2. (a) First and second integrations of EPR spectra of Pt/P25 with and without *in situ* light irradiations at room temperature (RT). (b) Time-resolved decay spectra of Pt/P25 at various temperature. (c-d) First and second integrations of EPR spectra of Pt/P25 with *in situ* light irradiations at elevated temperature. Temperature dependence of enhancement from EHC in the photothermal catalytic processes: (e) enhanced TOF and H₂/CO in DRM and (f) enhanced electron transfer and CH₄ selectivity in CO₂ reduction with H₂. (In e-f, X-temperature is referred to external heating temperature of photothermal catalysis).

lifetime of hot carriers with temperature, indicating that the accumulation region of hot carriers is changed from the metal-support interface at room temperature to metal surface at higher temperature.

3.3. Promotion effect of thermal energy on hot carriers

The enhanced TOF from EHC at various external heating temperature was first evaluated in photothermal catalytic DRM (Fig. 2e and Table S2-5). The reaction rate is predominantly contributed by the photo-induced EHC without external thermal energy, as thermocatalytic performances at both the same external furnace temperature with photothermal catalysis (room temperature) and catalyst surface temperature with photothermal catalysis (236 °C) are sluggish [4,19]. In the meantime, we conducted thermocatalysis by setting the catalyst bed temperature at the same catalyst temperature with photothermal catalysis to rule out the influence of thermal energy itself on the contribution of EHC [19]. Although this temperature measurement method may not detect the accurate temperature of catalyst surface after light irradiations, the results can still be used to study the various EHC contributions at different external heating temperature. With an increase of external heating temperature in photothermal catalysis (furnace temperature), a nearly linear growth in TOF with EHC was observed at low (300 °C) and medium (500 °C) levels of furnace temperature, from 0.9 mol CO/(mol Pt)/s at room temperature to 2.2 mol CO/(mol Pt)/s at 500 °C (Fig. 2e). Correspondingly, a H₂/CO ratio with EHC is improved from 0.51 to 0.77, showing a great promotion of thermal energy on the selective output of EHC. A similar trend was also observed in the process of photothermal CO₂ reduction with H₂ (Fig. 2f and Table S6-9). For instance, an almost linear increase of the enhanced electron consumption by photo-generated EHC was obtained at a low furnace temperature range (100–300 °C). This demonstrates that the

external thermal energy could promote the output of EHC for reactions within a certain range.

Recalling the mobility change of hot carriers from room temperature to 300 °C (Fig. 2a, c, d), the trend is different from that of the participation or consumption of hot carriers in photothermal catalytic reactions (Fig. 2e, f). Therefore, the mobility of hot carriers might not be the determining factor of their improved contributions with the increased external thermal energy. On this occasion, we compare the number of thermal and photo excited hot electrons at different temperature (Fig. 3a). The number of thermal excited hot electrons is calculated using the Fermi-Dirac distribution (Fig. 3b). To obtain the number of photo excited hot electrons, we first evaluate the energy absorption (E) of a Pt planar film (10 nm thickness) at various temperature, which is done by combining the DFT and FEM calculations, as outlined in Section 2.6. Then the number (N) of photo excited electrons, is calculated using $N = E/(h\lambda/c)$, where h is the Plank constant, λ is the radiation wavelength, and c is the speed of light. The expression in the bracket represents the energy quantum possessed by a single photo. Taking a 10 nm Pt thin film as an example, elevating the reaction temperature can result in an increased number of photo-induced hot carriers from 3.7×10^{20} at 25 °C to 5.6×10^{20} m²/s at 600 °C (Fig. 3a). This is in stark contrast to the negligible enhancement effect of temperature on thermally excited hot electrons (Fig. 3b and S4). As such, the increased amount of photo-generated hot electrons at elevated temperature have much higher probability in participating in and facilitating the catalytic reactions than those at low temperature.

The temperature-dependent redox potentials of reactants in the DRM and RWGS processes are illustrated in Fig. 3c. With the reaction temperature rising, both the potential values of CO₂/CO and CO/CH₄ dropped, resulting in a reinforced potential difference between the energy of hot carriers and the redox potentials of reactants. The enhanced

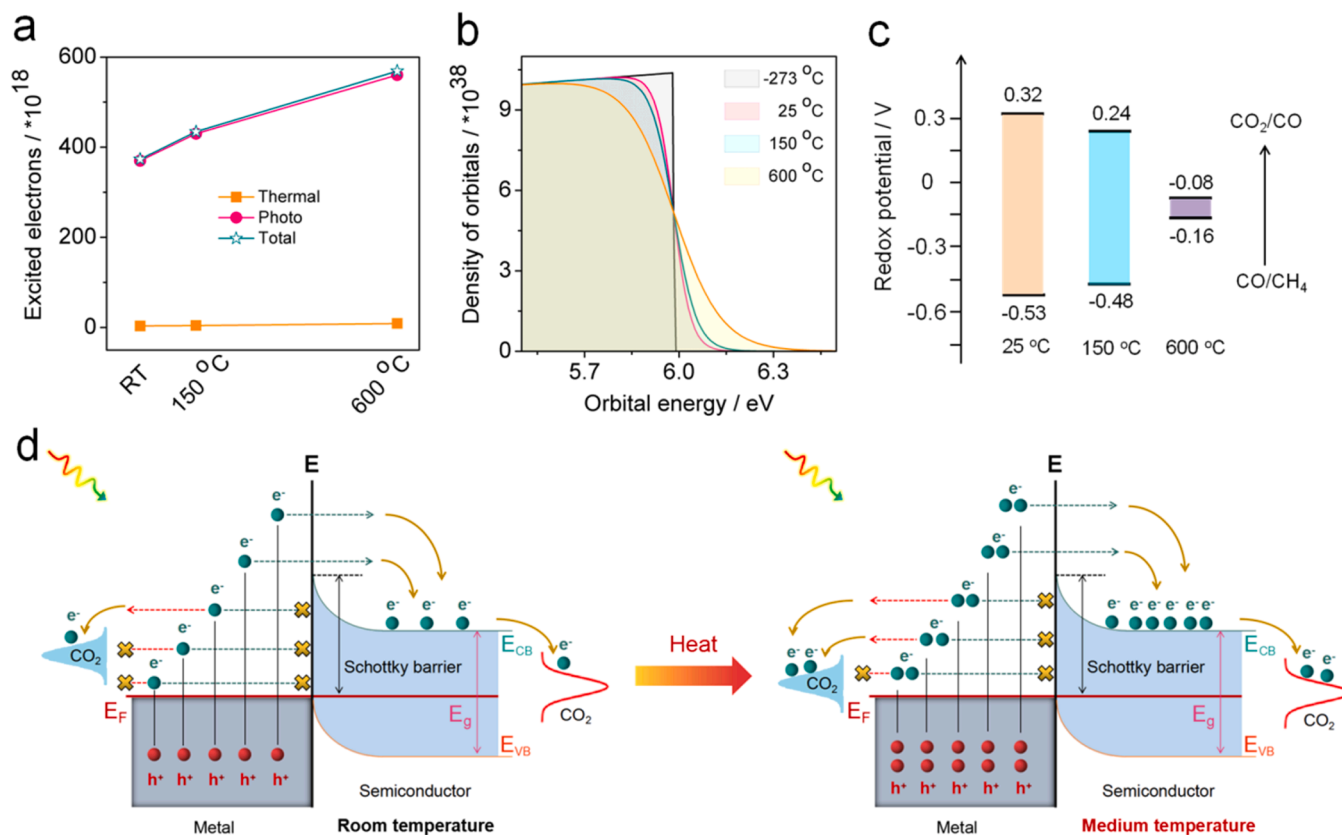


Fig. 3. Promotion of external thermal energy on the generation of hot carriers and their participation in redox reactions. (a–b) The generation amount of photo-excited and thermally excited hot carriers at different temperature. (c) The temperature effect on the redox potential of reactants in the processes of DRM and CO₂ reduction with H₂ process. (d) The schematic diagram of external thermal promotion effect on the behaviors of hot carriers.

driving force would easily lead to more EHC to participate in the redox reactions [34]. As a result, the larger number of photo-induced hot carriers and the lowered redox potentials of reactants at higher temperature contribute to the positive behaviors of EHC in photothermal catalysis (Fig. 3d).

To gain more insights into the thermal effect on EHC, we performed *in situ* diffuse reflectance infrared Fourier transform spectroscopy (DRIFTS) at varying temperature with and without light irradiations (Fig. 4a-b and S5). Without light illumination, no evidence of the initiation of DRM can be found at the furnace temperature of 150 °C. While in the presence of light only, both CO₂ and CH₄ can be activated, proven by the presence of HCO₃⁻ (1685/1420 cm⁻¹) [35], CO₃²⁻ (1557 cm⁻¹) [36], CO₂⁻ (1220 cm⁻¹) [37], COOH (1653 cm⁻¹) [38], and CH_x (2824/1440 cm⁻¹) [39] species. This fully demonstrates that the EHC are able to overcome the thermodynamic barrier of DRM. The EHC in photocatalytic DRM are involved into two pathways (Scheme S1): (1)

directly reducing CO₂ to CO with the intermediate of CO₂⁻; (2) converting CO₃²⁻ to COOH intermediate and then to CO. In the second pathway, H₂O as a by-product can be generated. At room temperature, a smaller number of EHC with enough energy were produced to overcome higher redox potentials of reactants, and most of EHC would prefer to participate in the second path, resulting in a lower H₂/CO ratio. With temperature increasing to 150 °C in photothermal catalytic DRM, the peak of CO₂⁻ turns stronger, while the peak intensity of other intermediates in the second pathway decreases. This suggests that the two pathways are boosted with more photo-induced EHC and lowered reduction potential of CO₂/CO, leading to an increased H₂/CO ratio. With temperature further rising above 300 °C, thermocatalytic DRM is also triggered. Especially at 500 °C, CO₃²⁻ and HCO₃⁻ can be converted to COOH by H radicals. After light was introduced, all the intermediates disappeared, meaning that both CO₃²⁻ and HCO₃⁻ can be rapidly converted to CO by EHC. In addition, less amount of water can be generated

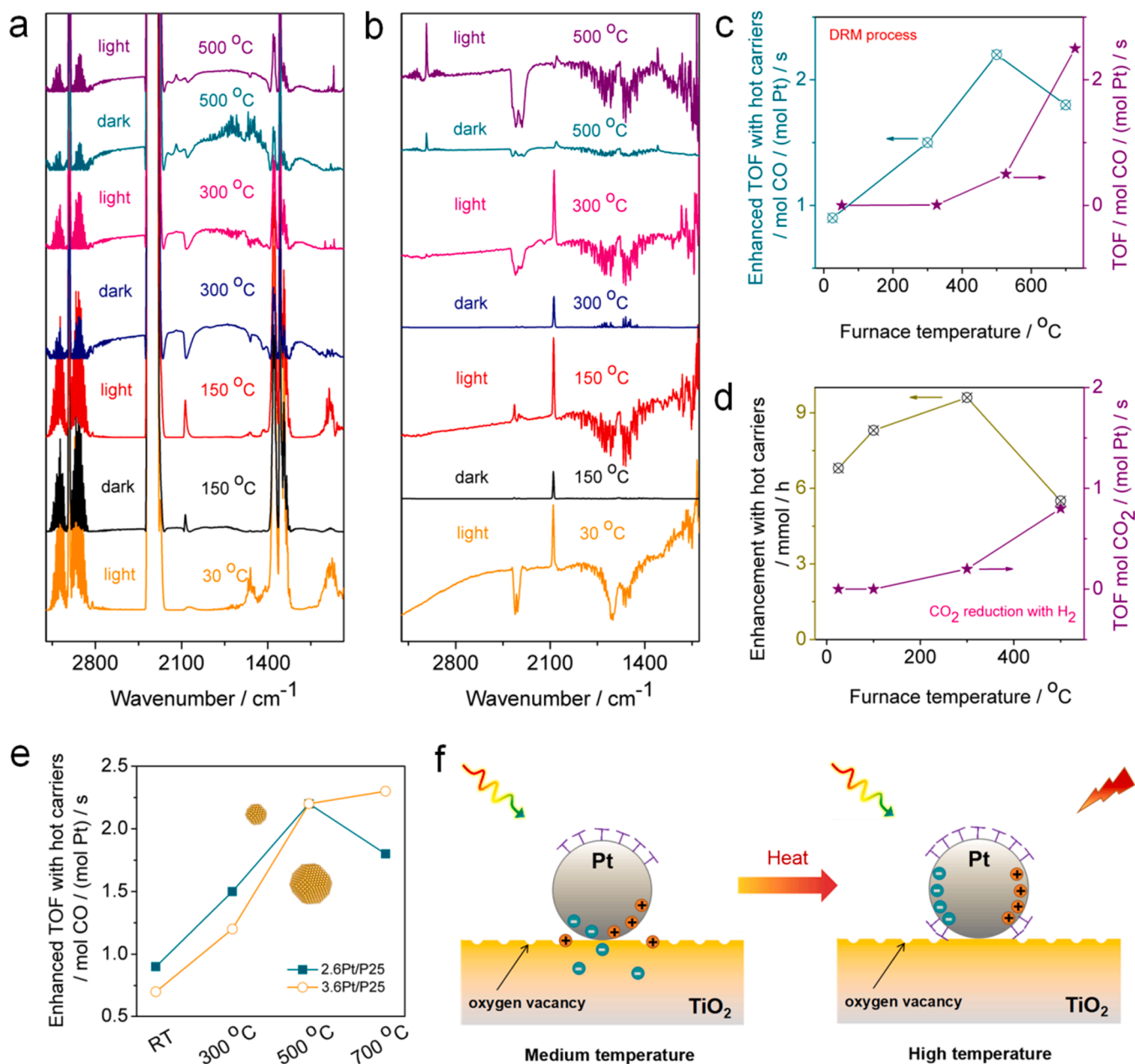


Fig. 4. *In situ* DRIFTS spectra with and without light irradiations in (a) DRM and (b) CO₂ reduction process with H₂. (c) Enhanced TOF with EHC and thermal assisted TOF at various temperature in DRM. (d) Enhanced electron transfer with EHC and thermal assisted TOF at various temperatures in CO₂ reduction process. (e) Enhanced TOF with EHC at various temperature on P25 supported different sized Pt NPs, and (f) the schematic diagram of thermal suppress effect on EHC.

after introduction of solar energy into thermocatalysis, as shown in the proposed reaction mechanism (Scheme S2-3), which is consistent with the improved H_2/CO ratio at high temperature.

In the CO_2 reduction with H_2 , COOH (1593 cm^{-1}) [39,40] is the main intermediate in photothermal catalysis. At low temperature (room temperature), most of EHC would like to convert COOH to CO rather than CH_4 , as the former process with one electron reaction is easier than the latter with four electrons process from the viewpoint of dynamics (Scheme S4). With furnace temperature being increased to 150°C and subsequent to 300°C , CHO (1067 cm^{-1}) [41], CH_2O (1795 cm^{-1}) [40], CH_3O (1103 cm^{-1}) [42], and CH_4 (1537 cm^{-1}) [39] species gradually turn apparently, indicating that the EHC prefer to selectively activate the CHO intermediates, promoting CH_4 production while minimally affecting the CO-metal bond for CO production (desorption) [21]. As a result, with temperature increasing from room condition to a medium level, more EHC can be excited by solar energy, together with the lowered redox potentials of reactants, a reinforced consumption rate of EHC and improved selectivity for targeted products (syngas from DRM and methane from CO_2 reduction with H_2) were both obtained (Fig. 3d).

3.4. Suppression effect of thermal energy on hot carriers

It is observed that TOF values on EHC and external thermal energy simultaneously increase in the photothermal catalytic DRM at low (300°C) and medium (500°C) levels of external heating temperature (Fig. 4c). As an uphill catalytic process, a growth of TOF in thermocatalysis remains with the temperature increasing up to 700°C , by contrast, a slight decrease appears for the TOF enhancement by EHC despite of the increased amount of EHC (Fig. 4c and Table S5). A similar phenomenon also occurs in the photothermal catalytic CO_2 reduction with H_2 (Fig. 4d and Table S9). When the reaction temperature rises from 300 to 500°C , the TOF in thermocatalysis keeps growing while there is a sharp decrease in the enhanced amount of transferred electrons by EHC. Especially, this suppression effect is more obvious in photothermal catalytic RWGS (Fig. S6), a thermodynamically endothermic process (Fig. S7). In the meantime, the same trends are found when we measure the number of consumed EHC with monochromatic light irradiations at different levels of external heating temperature. As the generated heat under monochromatic light irradiation can be ignored, thus fully verifying the suppression effect of thermal energy on the output of EHC at high temperature (Table S10).

Considering that the effective region of hot carriers is the metal surface at high temperature (proven above), we controlled the sizes of Pt QDs (2.6 and 3.6 nm) on P25 (Fig. S8) and compared their thermocatalytic performances and enhanced TOF with EHC (Table S11-13). Thermocatalytic DRM performance of $2.6\text{Pt}/\text{P25}$ is higher than $3.6\text{Pt}/\text{P25}$ throughout the temperature range. By contrast, the enhanced TOF by EHC on $2.6\text{Pt}/\text{P25}$ exceeds that on $3.6\text{Pt}/\text{P25}$ at low temperature while the trend turns oppositely at high temperature (Fig. 4e). The properties of Pt QDs on both the catalysts are almost the same except for the surface area. As observed from Eq. 5, the sum of active sites for photocatalysis and thermocatalysis is proportional to the surface area of Pt QDs, which is a constant. As such, the total active sites at low and medium temperature are unsaturated, thus the improvements on both the consumption of photo-induced EHC and the thermal contribution are acquired. However, no spare active sites on the catalysts are obtained at high temperature and more active sites are occupied for thermocatalysis as the thermodynamic barrier is overcome (Fig. S7). This leads to a smaller number of active sites available for photo-mediated catalysis, so the output of EHC is restrained [39] (Fig. 4f).

$$(A_p + A_t) \propto \text{surface area of Pt QDs} \quad (5)$$

Where, A_p and A_t represent the active sites of photocatalysis and thermocatalysis, respectively.

The conclusion can also be proven by *in situ* DRIFTS tests. In the

reaction of CO_2 reduction with H_2 , COOH can be acquired at 500°C with or without light (Scheme S5-6). This means the reaction pathway of thermocatalysis also occurs in photothermal catalysis, as such, a part of surface area is occupied by thermocatalysis, leaving a less region for the output of EHC. In addition, the peak intensity of CHO, CH_2O and CH_3O intermediates in photothermal catalysis (500°C) turns higher compared with thermocatalysis (500°C), demonstrating that more EHC would be selectively used for the formation of CH_4 , and thus a less contribution of the EHC in the RWGS process would be made at high reaction temperature.

3.5. Photothermal catalytic performance

As inspired by the thermal effect, *i.e.*, the promotion at low and medium temperature zones and the suppression at higher external heating temperature, on the EHC, the optimized quantum efficiencies of DRM and RWGS are both acquired at medium temperature levels, which are 500 and 400°C , respectively. The QE values at 420 nm reached as high as 56% and 20% in DRM and RWGS, respectively. Even at the wavelength of 500 nm , their QEs still remained to be 35% and 15% , respectively (Fig. 5a-b and Table S10), showing a great improvement in full utilization of solar light. Photothermal catalytic throughput not only considers the involvement of EHC, but also the thermocatalytic performance. As thermocatalytic performance has a direct relationship with temperature, the photothermal catalytic activities of DRM and RWGS processes are generally higher at high temperature, as shown by the TOF of 5.1 mol CO/h/g at 700°C and $1.0\text{ mol CO}/(\text{mol Pt})/\text{s}$ of RWGS at 500°C , respectively (Fig. 5c-d). These performances outperform the previous works (Table S14-15). Nevertheless, the synergy of solar and thermal energies in photothermal catalysis reaches the maximum at medium external temperature. In the meantime, we derived the activation energies of DRM and RWGS processes, which show significant decreases from 67.1 and 47.7 kJ/mol to 13.4 and 2.5 kJ/mol , respectively, after the addition of solar energy. The results suggest that the combination of solar energy and external heating can effectively reduce the reaction barriers (Fig. 5e-f). Meanwhile, at high external heating temperature, the enhancement from light irradiation in both DRM and CO_2 reduction reactions can be well reproducible (Fig. 5g and S9a). It was also of great interest to find that the catalyst stability under both external heating and light irradiation is comparable to that under thermocatalysis (Fig. 5h and S9b), showing the promising application of photothermal catalysis.

4. Conclusions

We have illustrated the external thermal effect on EHC in photothermal catalytic systems. With reaction temperature increasing, the hot region of Pt/P25 changes from metal-support interface to metal QDs surface. Meanwhile, a promotion at low to medium temperature and suppression effect at high temperature from external heating on EHC is experimentally and theoretically unveiled. Thermal energy will increase the generation of EHC and reduce the redox potentials of reactants to promote their participation in a reaction for the target products. When the reaction temperature is high enough to exceed the minimum onset temperature of conventional thermocatalysis, the active sites on metal surface would be mostly occupied by thermocatalysis, leaving a less output channel for hot carriers. Due to the promotion and suppression of thermal effects, the quantum efficiency of DRM and RWGS processes can reach the optimum at medium temperature, *e.g.*, 56% at 500°C and 20% at 400°C under 420 nm , respectively. The photothermal catalytic throughput attains a higher level at higher temperature as a result of thermocatalysis, with the TOFs of DRM and RWGS at $5.1\text{ mol CO}/(\text{mol Pt})/\text{s}$ at 700°C and $1.0\text{ mol CO}/(\text{mol Pt})/\text{s}$ at 500°C , respectively, while the synergy of solar and thermal energies reaches the maximum at medium temperature. This work unveils the key interaction in photothermal catalysis, which sheds light on the rational and industrial

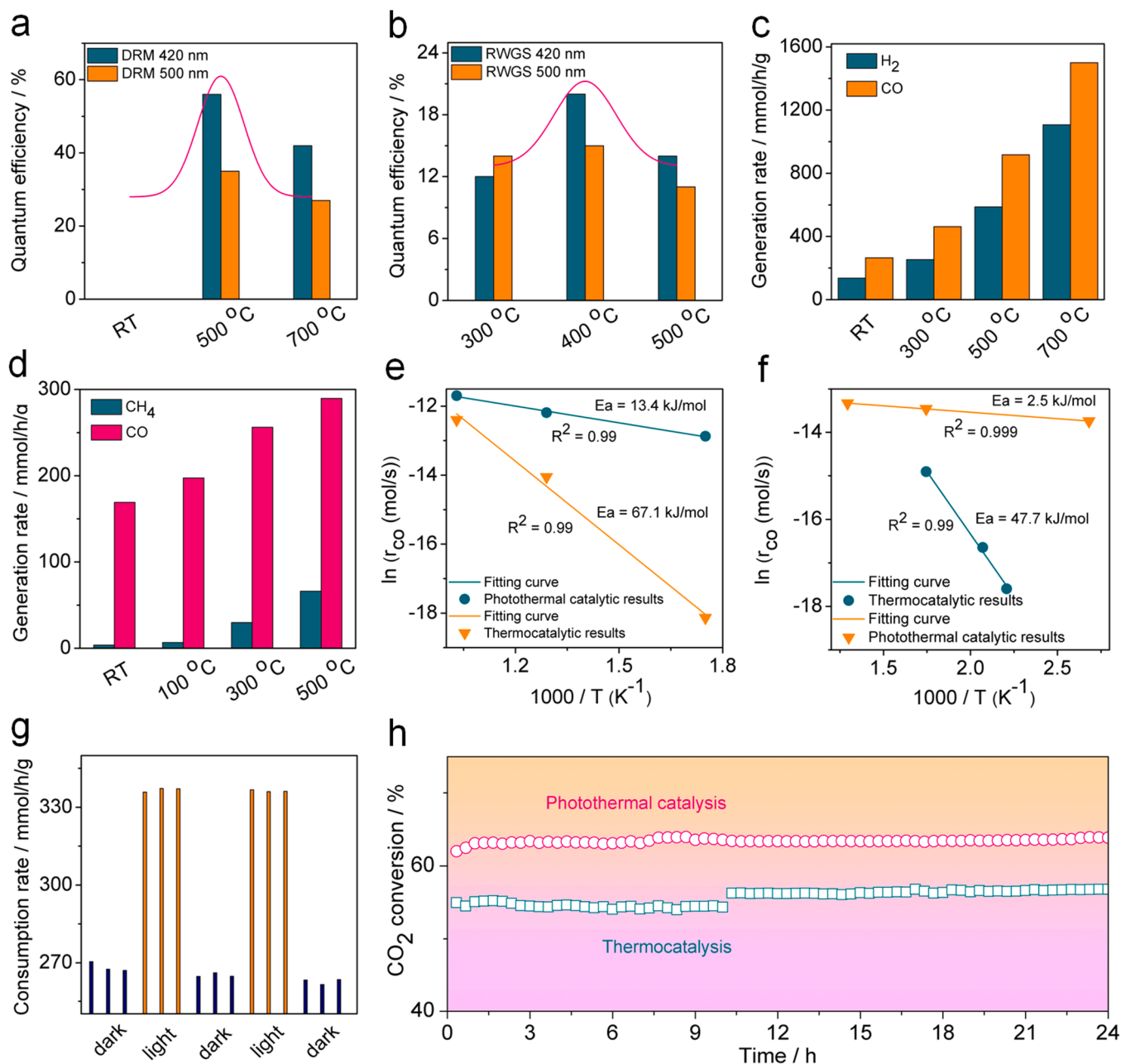


Fig. 5. Photothermal catalytic performances on Pt/P25 catalysts. Optimized quantum efficiencies under 420 and 500 nm in photothermal catalytic (a) DRM and (b) RWGS. The red lines are the fitted curves of bar graph, which represent the trends of quantum efficiency with external heating temperature. Photothermal catalytic throughput in photothermal catalytic (c) DRM and (d) CO₂ reduction reaction. Comparison of activation energy of thermocatalysis and photothermal catalysis in (e) DRM and (f) RWGS. (g) The reproducibility of EHC contribution at high external heating temperature with light being turned on and off and (h) the stability of photothermal catalytic performance in CO₂ reduction reaction within 24 h.

utilization of solar energy.

CRediT authorship contribution statement

Jinqiang Zhang: Conceptualization, Methodology, Data curation, Writing – original draft. **Yunguo Li:** Software, Investigation. **Jiaming Sun:** Data curation. **Haijun Chen:** Resources, Funding acquisition, Supervision. **Yuezhuo Zhu:** Conceptualization, Resources. **Xiaoli Zhao:** Software, Investigation. **Lai-Chang Zhang:** Supervision. **Shuaijun Wang:** Methodology. **Huayang Zhang:** Methodology. **Xiaoguang Duan:** Methodology. **Lei Shi:** Data curation, Resources. **Shu Zhang:** Data curation, Resources. **Peng Zhang:** Methodology, Resources. **Guosheng Shao:** Methodology, Resources. **Mingbo Wu:** Resources,

Conceptualization. **Shaobin Wang:** Funding acquisition, Data curation, Supervision. **Hongqi Sun:** Project administration, Funding acquisition, Writing – review & editing, Supervision.

Declaration of Competing Interest

The authors declare that they have no known competing financial interests or personal relationships that could have appeared to influence the work reported in this paper.

Acknowledgements

The author (H. Sun) would like to thank the support from the ECU

Vice-Chancellor's Professorial Research Fellowship. The support from the National Natural Science Foundation of China (51676096) is acknowledged. This work was partially supported by the Australian Research Council (DP170104264 and DP190103548). The authors acknowledge the equipment and assistance of The University of Western Australia Centre for Microscopy, Characterisation and Analysis, and the WA X-Ray Surface Analysis Facility of Curtin University, funded by an Australian Research Council LIEF grant (LE120100026).

Appendix A. Supporting information

Supplementary data associated with this article can be found in the online version at doi:10.1016/j.apcatb.2022.121263.

References

- [1] A. Fujishima, K. Honda, Electrochemical photolysis of water at a semiconductor electrode, *Nature* 238 (1972) 37–38.
- [2] X. Wang, K. Maeda, A. Thomas, K. Takanebe, G. Xin, J.M. Carlsson, K. Domen, M. Antonietti, A metal-free polymeric photocatalyst for hydrogen production from water under visible light, *Nat. Mater.* 8 (2008) 76–80.
- [3] S. Yu, X.B. Fan, X. Wang, J. Li, Q. Zhang, A. Xia, S. Wei, L.Z. Wu, Y. Zhou, G. R. Patzke, Efficient photocatalytic hydrogen evolution with ligand engineered all-inorganic InP and InP/ZnS colloidal quantum dots, *Nat. Commun.* 9 (2018) 4009.
- [4] L. Zhou, D.F. Swearer, C. Zhang, H. Robatjazi, H. Zhao, L. Henderson, L. Dong, P. Christopher, E.A. Carter, P. Nordlander, N.J. Halas, Quantifying hot carrier and thermal contributions in plasmonic photocatalysis, *Science* 362 (2018) 69–72.
- [5] H. Song, X. Meng, Z.-J. Wang, H. Liu, J. Ye, Solar-energy-mediated methane conversion, *Joule* 3 (2019) 1606–1636.
- [6] D. Mateo, J.L. Cerrillo, S. Durini, J. Gascon, Fundamentals and applications of photo-thermal catalysis, *Chem. Soc. Rev.* 50 (2021) 2173–2210.
- [7] H. Liu, X. Meng, T.D. Dao, H. Zhang, P. Li, K. Chang, T. Wang, M. Li, T. Nagao, J. Ye, Conversion of carbon dioxide by methane reforming under visible-light irradiation: surface-plasmon-mediated nonpolar molecule activation, *Angew. Chem. Int. Ed.* 54 (2015) 11545–11549.
- [8] J.M. Luther, P.K. Jain, T. Ewers, A.P. Alivisatos, Localized surface plasmon resonances arising from free carriers in doped quantum dots, *Nat. Mater.* 10 (2011) 361–366.
- [9] C. Han, S.H. Li, Z.R. Tang, Y.J. Xu, Tunable plasmonic core-shell heterostructure design for broadband light driven catalysis, *Chem. Sci.* 9 (2018) 8914–8922.
- [10] X.-Y. Lin, J.-Y. Li, M.-Y. Qi, Z.-R. Tang, Y.-J. Xu, Methane conversion over artificial photocatalysts, *Catal. Commun.* 159 (2021) 106346–106356.
- [11] N. Zhang, C. Han, X. Fu, Y.-J. Xu, Function-oriented engineering of metal-based nanohybrids for photoredox catalysis: exerting plasmonic effect and beyond, *Chem* 4 (2018) 1832–1861.
- [12] H.-K. Wu, F. Zhang, J.-Y. Li, Z.-R. Tang, Y.-J. Xu, Photo-driven Fischer–Tropsch synthesis, *J. Mater. Chem. A* 8 (2020) 24253–24266.
- [13] F. Zhang, Y.-H. Li, M.-Y. Qi, Y.M.A. Yamada, M. Anpo, Z.-R. Tang, Y.-J. Xu, Photothermal catalytic CO₂ reduction over nanomaterials, *Chem. Catal.* 1 (2021) 272–297.
- [14] A.O. Govorov, H.H. Richardson, Generating heat with metal nanoparticles, *Nano Today* 2 (2007) 30–38.
- [15] S. Shoji, X. Peng, A. Yamaguchi, R. Watanabe, C. Fukuhara, Y. Cho, T. Yamamoto, S. Matsumura, M.-W. Yu, S. Ishii, T. Fujita, H. Abe, M. Miyachi, Photocatalytic uphill conversion of natural gas beyond the limitation of thermal reaction systems, *Nat. Catal.* 3 (2020) 148–153.
- [16] C. Song, Z. Wang, Z. Yin, D. Xiao, D. Ma, Principles and applications of photothermal catalysis, *Chem. Catal.* 2 (2022) 52–83.
- [17] X. Meng, T. Wang, L. Liu, S. Ouyang, P. Li, H. Hu, T. Kako, H. Iwai, A. Tanaka, J. Ye, Photothermal conversion of CO₂ into CH₄ with H₂ over Group VIII nanocatalysts: an alternative approach for solar fuel production, *Angew. Chem. Int. Ed.* 53 (2014) 11478–11482.
- [18] X. Meng, L. Liu, S. Ouyang, H. Xu, D. Wang, N. Zhao, J. Ye, Nanometals for solar-to-chemical energy conversion: from semiconductor-based photocatalysis to plasmon-mediated photocatalysis and photo-thermocatalysis, *Adv. Mater.* 28 (2016) 6781–6803.
- [19] L. Zhou, J.M.P. Martinez, J. Finzel, C. Zhang, D.F. Swearer, S. Tian, H. Robatjazi, M. Lou, L. Dong, L. Henderson, P. Christopher, E.A. Carter, P. Nordlander, N. J. Halas, Light-driven methane dry reforming with single atomic site antenna-reactor plasmonic photocatalysts, *Nat. Energy* 5 (2020) 61–70.
- [20] J. Jia, P.G. O'Brien, L. He, Q. Qiao, T. Fei, L.M. Reyes, T.E. Burrow, Y. Dong, K. Liao, M. Varela, S.J. Pennycook, M. Hmadeh, A.S. Helmy, N.P. Kherani, D. D. Perovic, G.A. Ozin, Visible and near-infrared photothermal catalyzed hydrogenation of gaseous CO₂ over nanostructured Pd@Nb₂O₅, *Adv. Sci.* 3 (2016), 1600189.
- [21] X. Zhang, X. Li, D. Zhang, N.Q. Su, W. Yang, H.O. Everitt, J. Liu, Product selectivity in plasmonic photocatalysis for carbon dioxide hydrogenation, *Nat. Commun.* 8 (2017) 14542.
- [22] Z.F. Bian, S. Das, M.H. Wai, P. Hongmanom, S. Kawi, A review on bimetallic nickel-based catalysts for CO₂ reforming of methane, *Chemphyschem* 18 (2017) 3117–3134.
- [23] M. Cai, Z. Wu, Z. Li, L. Wang, W. Sun, A.A. Tountas, C. Li, S. Wang, K. Feng, A.-B. Xu, S. Tang, A. Tavasoli, M. Peng, W. Liu, A.S. Helmy, L. He, G.A. Ozin, X. Zhang, Greenhouse-inspired supra-photothermal CO₂ catalysis, *Nat. Energy* 6 (2021) 807–814.
- [24] S.S. Chen, T. Takata, K. Domen, Particulate photocatalysts for overall water splitting, *Nat. Rev. Mater.* 2 (2017) 17.
- [25] X.G. Duan, Z.M. Ao, H.Q. Sun, L. Zhou, G.X. Wang, S.B. Wang, Insights into N-doping in single-walled carbon nanotubes for enhanced activation of superoxides: a mechanistic study, *Chem. Commun.* 51 (2015) 15249–15252.
- [26] H. Song, X. Meng, T.D. Dao, W. Zhou, H. Liu, L. Shi, H. Zhang, T. Nagao, T. Kako, J. Ye, Light-enhanced carbon dioxide activation and conversion by effective plasmonic coupling effect of Pt and Au nanoparticles, *ACS Appl. Mater. Interfaces* 10 (2018) 408–416.
- [27] Y. Chen, Y. Feng, L. Li, J. Liu, X. Pan, W. Liu, F. Wei, Y.-T. Cui, B. Qiao, X. Sun, X. Li, J. Lin, S. Lin, X. Wang, T. Zhang, Identification of active sites on high-performance Pt/Al₂O₃ catalyst for cryogenic CO oxidation, *ACS Catal.* 10 (2020) 8815–8824.
- [28] C. Dong, C. Lian, S. Hu, Z. Deng, J. Gong, M. Li, H. Liu, M. Xing, J. Zhang, Size-dependent activity and selectivity of carbon dioxide photocatalytic reduction over platinum nanoparticles, *Nat. Commun.* 9 (2018) 1252.
- [29] M.I. Stockman, K. Kneipp, S.I. Bozhevolnyi, S. Saha, A. Dutta, J. Ndukaife, N. Kinsey, H. Reddy, U. Guler, V.M. Shalae, A. Boltasseva, B. Gholipour, H.N. S. Krishnamoorthy, K.F. MacDonald, C. Soci, N.I. Zheludev, V. Savinov, R. Singh, P. Groß, C. Lienau, M. Vada, M.L. Solomon, D.R. Barton, M. Lawrence, J. A. Dionne, S.V. Boriskina, R. Esteban, J. Aizpurua, X. Zhang, S. Yang, D. Wang, W. Wang, T.W. Odom, N. Accanto, P.M. de Roque, I.M. Hancu, L. Piatkowski, N. F. van Hulst, M.F. Kling, Roadmap on plasmonics, *J. Opt.* 20 (2018), 043001.
- [30] C. Mao, H. Li, H. Gu, J. Wang, Y. Zou, G. Qi, J. Xu, F. Deng, W. Shen, J. Li, S. Liu, J. Zhao, L. Zhang, Beyond the thermal equilibrium limit of ammonia synthesis with dual temperature zone catalyst powered by solar light, *Chem* 5 (2019) 2702–2717.
- [31] P. Zhang, Y. Li, Y. Zhang, R. Hou, X. Zhang, C. Xue, S. Wang, B. Zhu, N. Li, G. Shao, Photogenerated electron transfer process in heterojunctions: in situ irradiation XPS, *Small Methods* (2020), 2000214.
- [32] H. Song, X. Meng, Z.-J. Wang, Z. Wang, H. Chen, Y. Weng, F. Ichihara, M. Oshikiri, T. Kako, J. Ye, Visible-light-mediated methane activation for steam methane reforming under mild conditions: a case study of Rh/TiO₂ catalysts, *ACS Catal.* 8 (2018) 7556–7565.
- [33] J. Zhang, Y. Li, X. Zhao, H. Zhang, L. Wang, H. Chen, S. Wang, X. Xu, L. Shi, L.-C. Zhang, J.-P. Veder, S. Zhao, G. Nealon, M. Wu, S. Wang, H. Sun, A hydrogen-initiated chemical epitaxial growth strategy for in-plane heterostructured photocatalyst, *ACS Nano* 14 (2020) 17505–17514.
- [34] H. Yao, Y. Cui, D. Qian, C.S. Ponseca, A. Honarfar, Y. Xu, J. Xin, Z. Chen, L. Hong, B. Gao, R. Yu, Y. Zu, W. Ma, P. Chhabra, T. Pullerits, A. Yartsev, F. Gao, J. Hou, 14.7% efficiency organic photovoltaic cells enabled by active materials with a large electrostatic potential difference, *J. Am. Chem. Soc.* 141 (2019) 7743–7750.
- [35] Z. Jiang, H. Sun, T. Wang, B. Wang, W. Wei, H. Li, S. Yuan, T. An, H. Zhao, J. Yu, P. K. Wong, Nature-based catalyst for visible-light-driven photocatalytic CO₂ reduction, *Energy Environ. Sci.* 11 (2018) 2382–2389.
- [36] M. Németh, D. Srankó, J. Károlyi, F. Somodi, Z. Schay, G. Sáfrán, I. Sajó, A. Horváth, Na-promoted Ni/ZrO₂ dry reforming catalyst with high efficiency: details of Na₂O-ZrO₂-Ni interaction controlling activity and coke formation, *Catal. Sci. Technol.* 7 (2017) 5386–5401.
- [37] L. Liu, C. Zhao, Y. Li, Spontaneous dissociation of CO₂ to CO on defective surface of Cu(I)/TiO_{2-x} nanoparticles at room temperature, *J. Phys. Chem. C* 116 (2012) 7904–7912.
- [38] N.J. Firet, W.A. Smith, Probing the reaction mechanism of CO₂ electroreduction over Ag films via operando infrared spectroscopy, *ACS Catal.* 7 (2016) 606–612.
- [39] W. Jiang, J. Low, K. Mao, D. Duan, S. Chen, W. Liu, C.-W. Pao, J. Ma, S. Sang, C. Shu, X. Zhan, Z. Qi, H. Zhang, Z. Liu, X. Wu, R. Long, L. Song, Y. Xiong, Pd-modified ZnO-Au enabling alkoxy intermediates formation and dehydrogenation for photocatalytic conversion of methane to ethylene, *J. Am. Chem. Soc.* 143 (2020) 269–278.
- [40] B. Xie, R.J. Wong, T.H. Tan, M. Higham, E.K. Gibson, D. Decarolis, J. Callison, K.-F. Aguey-Zinsou, M. Bowker, C.R.A. Catlow, J. Scott, R. Amal, Synergistic ultraviolet and visible light photoactivation enables intensified low-temperature methanol synthesis over copper/zinc oxide/alumina, *Nat. Commun.* 11 (2020) 1615.
- [41] X. Li, Y. Sun, J. Xu, Y. Shao, J. Wu, X. Xu, Y. Pan, H. Ju, J. Zhu, Y. Xie, Selective visible-light-driven photocatalytic CO₂ reduction to CH₄ mediated by atomically thin CuInS₂ layers, *Nat. Energy* 4 (2019) 690–699.
- [42] Z. Liu, S. Yao, A. Johnston-Peck, W. Xu, J.A. Rodriguez, S.D. Senanayake, Methanol steam reforming over Ni-CeO₂ model and powder catalysts: Pathways to high stability and selectivity for H₂/CO₂ production, *Catal. Today* 311 (2018) 74–80.